5-2017

PLANT IMAGE PROCESSING: 3D VOLUME RECONSTRUCTION, HYPERSPECTRAL INFORMATION MINING AND VISUALIZATION

Shi Cao
University of Nebraska-Lincoln, caoshi86@gmail.com

PLANT IMAGE PROCESSING: 3D VOLUME RECONSTRUCTION, HYPERSPECTRAL INFORMATION MINING AND VISUALIZATION

by

Shi Cao

A THESIS

Presented to the Faculty of

The Graduate College at the University of Nebraska

In Partial Fulfilment of Requirements

For the Degree of Master of Science

Major: Computer Science

Under the Supervision of Hongfeng Yu

Lincoln, Nebraska

May, 2017

PLANT IMAGE PROCESSING: 3D VOLUME RECONSTRUCTION, HYPERSPECTRAL INFORMATION MINING AND VISUALIZATION

Shi Cao, M.S.

University of Nebraska, 2017

Adviser: Hongfeng Yu

Image processing techniques have been widely used in plant science for plant phenotyping studies. These fast algorithms are desired to process massive image data. In this thesis, we analyze RGB digital images taken from different view angles of plants and propose an efficient ad-hoc algorithm to identify structures of plants by 3D volume reconstruction techniques. We study hyperspectral images of plants and extend our scope to other images from different scientific disciplines. Obtaining the spectral and spatial information simultaneously is a challenging task due to the high dimensionality of hyperspectral images. We first develop a real-time interactive tool for exploring the hyperspectral images as a hyperspectral data cube. We discover a strong correlation between information entropy and hyperspectral images with respect to the wavelength under which the hyperspectral images are taken. We design an information metric based transfer function allowing users to study the hyperspectral data cube by interactive volume rendering techniques. In this manner, the transfer function changes dynamically with the regions of interest selected by users and both the spatial and spectral information can be preserved. We show the usefulness of our approach in different scientific disciplines including plant science, physics and remote sensing. In addition, our transfer function also works for the traditional volumetric data and our method provides a new interactive way of volume rendering.

ACKNOWLEDGMENTS

I am very grateful to my adviser Prof. Hongfeng Yu for providing me the great opportunity to be a research assistant in Computer Science Department. What make the work in this thesis possible are Prof. Yu's supervision and guidance. His criticisms and suggestions keep me working hard and towards to right directions.

Thanks to the kind and selfless help from our group members Feiyu Zhu, Lina Yu, Jianping Zeng as well as helpful discussions with Jieting Wu and Babak Jafarisamani, I can participate into different projects gaining the experiences of image processing and visualization techniques in approximately eight months in Prof. Yu's group. I am impressed and inspired by their expertise, diligence and tireless effort.

This research has been sponsored in part by the National Science Foundation through grants DBI-1564621, IIS-1423487 and ICER-1541043.

I would like to thank Prof. Sheng Wei and Prof. Lisong Xu for being my committee members as well as their suggestions and advice to this work.

I would also like to thank Prof. Peter Dowben who is my PhD advisor in Physics Department and offers me tremendous support in pursuing this degree. In this work, a physics data set ($LuFeO_3$ PEEM images) has been studied. I would like to give acknowledgement to Prof. Xiaoshan Xu for growing the $LuFeO_3$ sample and to Canadian Light Source as well as Dr. Jian Wang there for the help of taking data. The experiment on physics data was also supported by the National Science Foundation through NSF-ECCS1508541 and the Nebraska Polarization and Spin Phenomena in Nanoferroic Structures (P-SPINS) MRSEC NSF DMR-1420645.

I wish to acknowledge our collaborators Prof. Harkamal Walia and his group members

as well as plant phenotyping facilities manage Dr. Vincent Stoerger for providing the plant image data and other help.

I appreciate the policy of the graduate school of University of Nebraska-Lincoln allowing students to participate into two graduate programs at the same time, which eventually makes this thesis possible from the beginning.

Last but not least, I am grateful that I received unconditional support from my family during these years. With their love, I will keep going forward.

Contents

List of Figures

Chapter 1

Introduction

One of the key objectives that plant scientist and agriculturist want to achieve is to ensure the crop production is sufficient for the growing population. The goal is challenging because current rate of increase of crop yields is lower than the increased demand for food and fuel [16]. A promising approach is selecting high yielding, stress-tolerant plants through the study of genotype and phenotype. The genotype, known as DNA sequence of the genetic makeup of an organism, with inherited epigenetic factors and non-inherited environmental factors determine the phenotype. The plant phenotype consisting of complex traits (such as, growth, development, tolerance, resistance and so on) provides a comprehensive assessment of these traits. However, the lack of effective and reliable phenotyping data limits the study of analyzing the genetics of quantitative traits that relate to growth, yield and adaptation to stress.

High throughput phenotyping studies of plants growing in controlled environments, such as growth chamber or greenhouse, have provided fast and inexpensive genomic information. The assessments of phenotype traits used to rely largely on visual scoring by domain experts, which is time-consuming and infeasible for extremely large scale studies [23]. The imaging based plant study opens up the possibility of high throughput pheno-

typing and leads to the development of many imaging platforms [23, 17]. The autonomous platforms can take images in near real-time at any stage during the plant growth, resulting in massive amounts of data for analysis. Modern imaging techniques allow for the visualization of multi-dimensional and multi-variable data that are used to quantify the growth, yield and applications to stress. The plant images are taken with a large range of wavelength of electromagnetic waves (light) due to the fact that plant leaves interact with light at different wavelength reflecting different information. For example, in the visible range (400-750 nm) of light, photoactive pigments (chlorophylls, anthocyanins, and carotenoids) dominates the interaction and in the near-infrared range (750-1200 nm) of light, multiple scattering at the air-cell interfaces in the internal leaf tissues causes high reflectance of light from plant leaves.

In this work, all plant image data is taken in a controlled environment (greenhouse). We focus on two types of images: visible light images known as RGB images, and hyperspectral images taken with wavelength of light from 550 nm to 1750 nm. RGB images are the digital images intending to mimic human perception to provide visual information about plant phenotype. The raw data of a RGB image is essentially a matrix M with dimension of $m_x \times m_y$, where indexes $(x \in m_x, y \in m_y)$ known as the pixel position represent the spatial locations and intensity values $M(x,y)$ associated with pixels (x,y) corresponds to photon fluxes in the red (600 nm), green (550 nm) and blue (450 nm) spectral bands of electromagnetic waves. RGB images encode plant morphology information and have a wide range of applications in the study of root system, seed surface features, leaf length and width [23, 17]. Hyperspectral images can be considered as an extension of RGB images with respect to a wavelength/band range of light. In hyperspectral imaging, *band* is more frequently used to represent $wavelength$ and they are used exchangeably. At a given band, one image is taken and across the entire band range, a series of images are obtained as hyperspectral images. The interaction between plants and light at different bands gives the

so-called spectral information of plants. Hyperspectral imaging, originally developed for remote sensing applications [32], is an emerging technique that integrates both spatial and spectral information. Hyperspectral images have been widely used in plant phenotyping studies [23, 24, 35] to discriminate genotypes with different contents of leaf biochemical components. The leaf chlorophyll (such as ref. [38, 3]) and thocyanins [13] or nitrogen [39] contents are different and a hyperspectral image provides a non-destructive, rapid and safe method of qualitative analysis of plants.

New imaging platforms and massive image data provide great opportunities to study plant phenotype. However, the challenge is obvious. The processing time for massive amounts of image data may become the bottleneck for high throughput phenotyping study. For example, in our data set, one RGB image with 2000×2000 pixels takes 4 MB of disk space. It is very common to take images at different view angles for continuous days. If images from 10 view angles for a plant are taken for 30 days then there are more than 1 GB RGB image data saved. In one experiment, plant scientists usually grow hundreds of plants to compare with the same number plants from one or more controlled group. There exists more than 100 GB data for just one experiment. In addition, the crop plants grow fast and vary day by day. The real-time analysis is desired and necessary.

In this thesis, our objective is to obtain growth information from RGB images and hyperspectral images for crop plants. Image processing techniques are applied to these images. Information mining and visualization of the hyperspectral images have not only been done for plant images but also for images from other scientific fileds. This thesis is organized as follow: Some related work of image processing and hyperspectral images are introduced in Chapter 2. From RGB images, we aim to get the structure information of plants by utilizing the three dimension (3D) reconstruction techniques. An ad-hoc solution is proposed to help plant scientists obtain the 3D structure of plants from RGB images taken at 5 different view angles. This part is introduced in Chapter 3. For hyperspectral

images, we make several technical contributions in developing a real-time interactive tool to explore the hyperspectral images by volume rendering. The hyperspectral image information mining and visualization are introduced in Chapter 4. In Chapter 5, the conclusions and future work are discussed.

Chapter 2

Related Work

2.1 Image processing in plant science

The functionality of plant imaging goes above and beyond taking images for plants. It is primarily used to measure traits of plant architecture such as biomass [14], imbibition and germination rates [11], yield [12], leaf morphology [18], seed morphology [8] and root architecture [10]. A series of image processing algorithms are used and developed to study plant images. The pre-processing methods such as contrast enhancement and noise removal algorithms are important. The variability of luminance issues such as sunlight and shadow can be addressed by image enhancement algorithms [19, 27]. Oriented Gaussian filters [6] are used to optimize the skeletonization of a plant image. The segmentation algorithms are necessary to divide an image into different regions of interest (ROIs), such as leafs, stems, roots and background which contains soil, pot and other residues. Background removal is an essential stage for avoiding any mis-classification. These algorithms use different approaches to make the segmentation. Examples include color index-based segmentation, threshold-based segmentation, and learning-based segmentation [17]. Once the ROIs from plants are identified, statistical work such as counting pixels or calculating areas can be

done.

However, plants grow in 3D space and the 2D image processing has certain limitations for exploring 3D plants. Although scientists can obtain information from 2D images in a relatively fast manner, a 2D image is a projection from a 3D plant, which may cause a loss of spatial information, especially when there is occlusion in the perception of a plant. In this situation the morphological analysis in 2D images is less intuitive than a 3D model. The 3D analysis has tremendous potentials in accurately estimating specific morphological features. There exists different ways to reconstruct a 3D model of an object from multiple views of 2D images [31, 22] and some are introduced to plant science to help plant scientists obtain 3D plant models. For example, GROWSCREEN 3D [5, 26] and the solution proposed by Wang *et al.* [36] focus on 3D leaf reconstruction and the RootReader3D software platform [10] gives the root reconstruction.

The plant 3D reconstruction by images from multiple angles at some circumstances is infeasible since the uniform color, thin leaf area and specular surface of plant leaves introduce challenges to typical reconstruction techniques. The solution addressing these problems can be reconstructing the structures instead of the leaves or the entire plants [6, 37]. Previous work [37] points out there actually are advantages for reconstructing a structure instead of the plant shape.

As we introduced above, there is existing work to reconstruct a 3D plant model. For the data set provided by our domain collaborators, we would like to conduct reconstruction of a 3D plant model in real-time. In Chapter 3, the detailed solutions are introduced.

2.2 The study of hyperspectral images

The hyperspectral images measure the interaction between light and materials. It is known that the electromagnetic waves (light) are categorized based on wavelength (which is of-

ten referred as a band in hyperspectral imaging) into many ranges such as X-ray, Ultraviolate(UV), Visible light (VIS), near infrared (NIR) and microwave, and so on. Materials interact with an electromagnetic wave in the basic forms, such as *absorption* and *reflection*. By analyzing the absorption on an atomic or molecular level, scientists can obtain the fingerprint of the materials. Researchers have developed a plenty of techniques to analyze hyperspectral images across different domains.

Hyperspectral images can be modeled as a three-dimensional (3D) data block known as a hyperspectral data cube. The X and Y dimensions reserve the spatial information of imaged objects and the X or λ dimension contains the spectrum information that acts like a fingerprint for objects shown in the X and Y space. The hyperspectral data cube is obtained by keeping the field of view of image fixed and stacking one image for one wavelength examined after another, stored as the Band Sequential (BSQ) format. Usually, a study of this 3D data cube consists of two individual parts: one is applying image fusion technique [30] to get a two-dimensional (2D) digital image with up to 3 channels (i.e., R, G, B); and another is studying the one dimensional (1D) spectra in one given region of interest (ROI) on the 2D image obtaining the intrinsic clustering information based on some distance measurements. However, the existing studies are relatively ad-hoc in that the fused 2D image and 1D spectral are studied and visualized individually, making it less effective and intuitive to correlate the spatial to spectral information. As a result, although many sophisticated methods have been presented, they often require users to exhaustively search appropriate parameters or leverage prior knowledge to identify features in a trial and error manner.

The most common method to reduce dimensions for a hyperspectral 3D cube is calculate the *reflectance indices* which are calculated from discrete bands among the entire typical wavelength range (400-2000 nm). The normalized difference vegetation index (NDVI)

is one of the popular indices [28]. It is calculated by

$$NDVI = \frac{(NIR - VIS)}{(NIR + VIS)} \tag{2.1}$$

where NIR and VIS are wavelengths typically chosen [25] as 770 nm and 670 nm in plant science. By calculating the index for each pixel (x, y) of images in these two bands, one can obtain the index map which can be interpreted as a 2D image fused from the entire cube data. With various indices, different 2D images are obtained for the same plant for studying different plant components [35].

In a physical or chemical analysis, usually Raman imaging is identified as one of the hyperspectral imaging techniques [15]. There exists other imaging techniques such as electron microscopy images taken by varying a spectral variable. The spectral variable can be incoming X-ray/UV light energy or electron kinetic energy resulting in images known as photoemission electron microscopy (PEEM) images or low energy electron microscopy (LEEM) [2] respectively. In our work, we show that our hyperspectral data model concept can be naturally extended to PEEM/LEEM or other similar images. Traditionally, one or several images with higher intensity are selected out from the entire image sequences for visualization and the spectral information (for example, X-ray absorption spectra obtained in X-ray PEEM images) are studied accordingly [7].

The hyperspectral imaging techniques were originally developed from remote sensing fields. There are numerous studies of fusing images from different bands to one single 2D image [30]. In addition to the reflectance indices (such as, NDVI) introduced above, other dimension reduction methods (such as principal component analysis (PCA) or discrete wavelet transform (DWT)) are commonly used for image fusion. For other image fusion techniques, usually one or more cost functions are constructed and minimizing of these functions results in the 2D image fusion [4]. One expects that a fused 2D image

keeps as much information as possible. The supervised or non-supervised learning of spectra is also developed to classify the regions in a 2D image based on the spectra or other properties.

As we introduced above, generally, hyperspectral images in various domains are studied following the same strategy: reduce the dimensions to generate a 2D image. In addition, the spectral analysis is performed individually as it is unfeasible to obtain information in all three dimensions of a hyperspectral cube simultaneously. In Chapter 4, the detailed solutions are introduced to tackle all these problems.

Chapter 3

Three-dimensional (3D) Reconstruction

3.1 The objective of plant 3D reconstruction

The images for this work are from rice and maize plants. For a given rice or maize plant, there are 5 images taken at different angles of 0°, 72°, 144°, 216° and 288°, respectively. The first pre-processing step is to crop the images since the plants only take a small portion of the entire original images which have a size of 2454×2056 pixels. A typical cropped image approximately has 500×500 pixels, which can reduce the entire reconstruction time.

For a complete plant shape reconstruction, more images from different angles with higher resolution are expected [21]. However, the structure reconstruction of plants in the similar imaging condition can be achieved [37]. In this work, we focus on obtaining the structure of plants.

We choose to implement the Shape-From-Silhouette (SFS) algorithm [9] to obtain a 3D model of plant. The principle of SFS estimating the shape of a object is that the back-projections from silhouette images taken at different angles of the same objects intersect with each other resulting in a *visual hull*. The schematic picture is shown in Fig. 3.1 to illustrate this. With W_i being a camera center and Ψ_i being a silhouette image, the

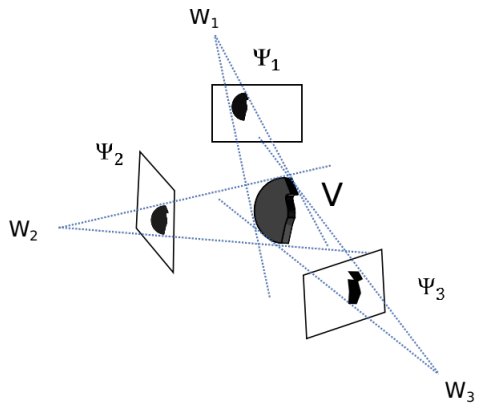

Figure 3.1: The Shape-From-Silhouette problem scenario: three silhouette images are projected from the camera centers backward. The obtained intersection V is the visual hull.

SFS algorithm gives the intersection part known as the visual hull which is an approximation 3D model of a real object [9]. It is worth pointing out that a silhouette image of an object literally means the main object of this image is in black (binary 0) and the background is in white (binary 1). While in practice the contrast is flipped which means the object is in white because usually the object only takes a small portion in an image and the white-object-black-background "silhouette" is more efficient with respect to memory space cost. Without specification, our silhouette or binary image follows the white-object-black-background style.

The plant leaves have relatively simple structures and specular surfaces. The green color of leaves is homogeneous and the contrast is large between plants and background. The information loss in silhouette is limited in this case. Once we compute the silhouette images of a plant, by implementing SFS algorithm, we can obtain a visual hull of the plant. However, the volume contained in a visual hull is a upper bound of a real plant. In Section 3.2, we propose an ad-hoc algorithm to obtain silhouette images and skeletons of plants from the obtained silhouette images. We show how we can obtain meaningful information from a visual hull for plant scientists.

3.2 3D volume and structure reconstruction of plants

Plant images are taken in a controlled environment. All plants are grown in pots sitting in front of a white board background. It is straight forward to get the segmentation of a plant and background by HSV values [34] in an image and then the binarization can be done by assigning the background as binary 0 and the foreground (plant) as 1. The obtained binary images can be considered as the silhouette images of the plant. The visual hull obtained from the silhouette images for a plant is a superset of a 3D model of the plant so that the shape information of plant is not accurate. However, the skeleton of a visual hull of a reconstructed plant can be considered as the structure of a plant. Plant scientists can obtain the length information of the leaves or stems for a plant. If a 3D skeletonization algorithm is applied to the visual hull, the 3D structure of a plant may be obtained. The problem of this solution is that the 3D skeletonization is a challenging problem and it is expensive and may not be optimized for our application [29].

We propose an ad-hoc algorithm (Algorithm 1) to obtain the silhouette and skeleton of a plant image in $O(N)$ time where N is the total number of pixels an image contains. For a RGB image, there are three channels and in this work we use the intensity value only from the blue channel, which is sufficient for us to distinct a plant from the white background. Our method is low-cost with respect to memory space due to the fact that we only use one channel and other methods based on HSV values [34] have to make use of all three channels. We split the channels directly and do not need to convert a RGB image to a gray image, which also reduces the computation cost. The plants from blue channels of images have lower intensity values compared with the white background and then an threshold can be used to segment plants and the white background. The basic idea of our algorithm is to use the local information of an image and for each row (the X direction) we identify the plant and the background. The advantage of using the row information is to overcome the

Algorithm 1 2D skeletonization

1: Initialize two 8-bit empty images Ψ_{sil} and Ψ_{bi} with size as input image Ψ
2: **for** each row $R \in$ image Ψ **do**
3: Get the mean value $Mean$ and standard deviation STD for the pixel values in R
4: **for** each pixel value $I_v \in R$ **do**
5: **if** $I_v < mean + \alpha * STD$ and $I_v < \beta$ **then** ▷ α and β are practical parameters
6: I_v is assigned to the plant
7: Set I_v as 255 ▷ White in 8-bits gray image
8: **else**
9: I_v is assigned to the background
10: Set I_v as 0 ▷ Black in 8-bits gray image
11: **end if**
12: Write I_v to the corresponding pixel in Ψ_{sil}
13: **end for**
14: **end for** ▷ The silhouette image Ψ_{sil} is obtained
15: **for** each row $R \in$ image Ψ_{sil} **do**
16: Find the regions corresponding to the plant
17: Find the boundary pairs which bound the regions
18: Find the midpoints (pixel positions) of these boundary pairs
19: Write 255 to the pixel positions of all midpoints to Ψ_{bi}
20: **end for**
21: **for** each column $C \in$ image Ψ_{sil} **do**
22: Find the regions corresponding to the plant
23: Find the boundary pairs that bound the regions
24: Find the midpoints (pixel positions) of these boundary pairs
25: Write 255 to the pixel positions of all midpoints to Ψ_{bi}
26: **end for**

problem introduced by the inhomogeneously distributed light background. The threshold can be obtained according to the mean value and standard deviation of a set of intensity values corresponding to a given row in the image. This step is shown in Line 4-13 of Algorithm 1. Once the segmentation is done for a plant and background we can obtain the silhouette image and also identify the edges of plant in both the X and Y directions of an image. An example is given in Fig. 3.2 (c) where the red pixels are the boundary pixels. In Algorithm 1 Line 15-20, we obtain the midpoints of plant boundaries along the X direction as shown by the yellow pixels in Fig. 3.2 (d). In Line 21-26 we obtain the midpoints of

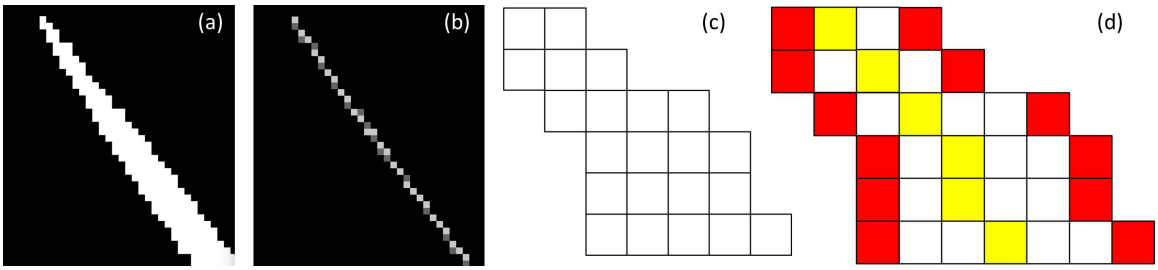

Figure 3.2: The schematic illustration of our 2D skeletonization algorithm for rice images. (a) shows a real rice plant leaf. (b) shows the obtained skeleton, where the brighter and darker pixels are from scanning along the X and Y directions, respectively. (c) shows a schematic illustration of an identified leaf region. (d) shows the midpoints (in yellow) of boundary pixels (in red) of an identify leaf regions along the X direction.

plant boundaries along the Y direction.

The reason that we can use a set of midpoints of a leaf region to represent a skeleton or structure of the leaf is straightforward. In our data set, all the leaves have simple geometry shapes and each leaf has a mirror plane along leaf main vein. As shown in Fig. 3.2 (a), the 2D leaf of rice has a symmetry axis approximately along the diagonal direction. In Fig. 3.2 (b), the obtained midpoints are shown and it can be regarded as a skeleton of Fig. 3.2 (a). A synthetic leaf region is shown in Fig. 3.2 (c). One white box with black boundaries represents a pixel in a real image. The boundaries of the synthetic leaf region are shown in red in Fig. 3.2 (d). The midpoints of these red boundaries are shown in yellow. Once the region of leaf is identified, we can scan the images to search the boundaries of leaf regions along both the X and Y directions. The midpoints corresponding to one pair of boundary points can be simply calculated. Except leaves, the stem of a plant is approximately a cylinder which also has very high symmetry. As a result, the highly symmetric structure of rice or maize makes our argument valid. The results of implementing our algorithm on rice data set are shown in Fig. 3.3.

From the silhouette images by implementing the SFS algorithm, the reconstructed 3D model of a plant can be obtained. In Fig. 3.4 (a), the top view of volume rendering result

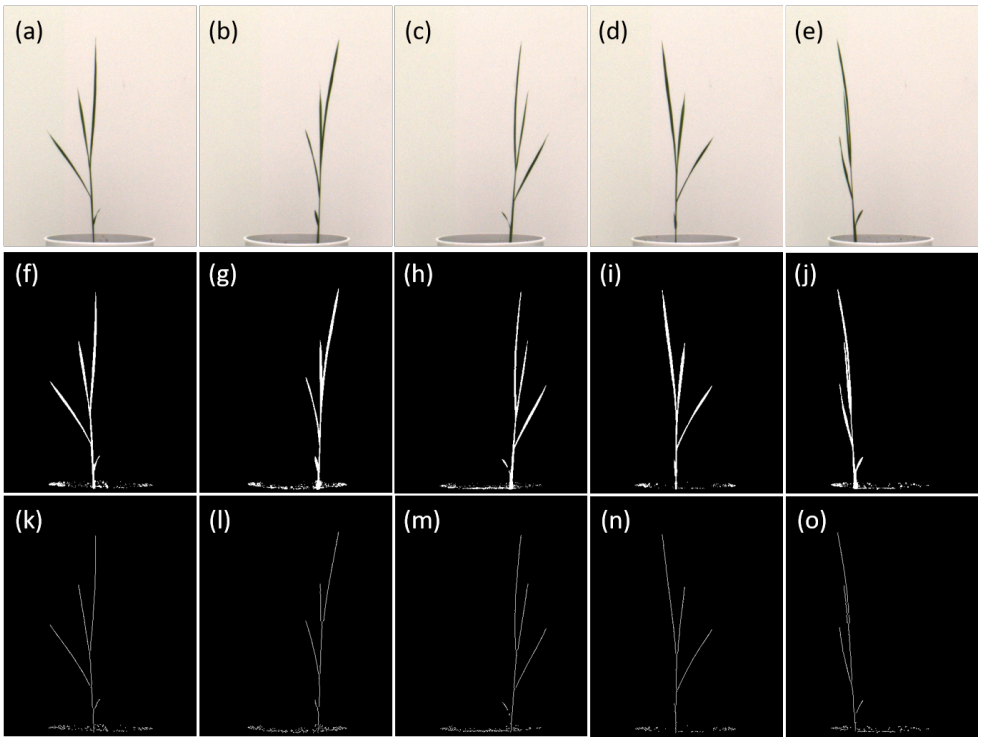

Figure 3.3: The results of our 2D skeletonization algorithm. (a)-(e) show the original input images from different angles. (f)-(j) show the silhouette/binary images. (k)-(o) show the skeletonized images.

indicates the principle of how the way of finding intersection from silhouette images works and there are 10 main components which can be identified. The side view is shown in Fig. 3.4 (b) and the visual hull is highlighted in green. If we only keep the visual hull visualized, it gives the approximation of a plant as shown in Fig. 3.4 (c).

The structure of a plant in a 3D model can be obtained by combining the 3D visual hull and 2D skeleton of a plant. Among all the skeletons from different view angles shown in Fig. 3.3 (k)-(o), a skeleton with maximum pixel numbers is automatically recommended to users and the intersection of this skeleton with the 3D visual hull leads to a 3D structure. The intersection of the visual hull in Fig. 3.4 (c) and the skeleton in Fig. 3.3 (m) is the approximation of 3D structure of this plant shown in Fig. 3.4.

The rice plants have simple structures in our data set. Our approach can be naturally

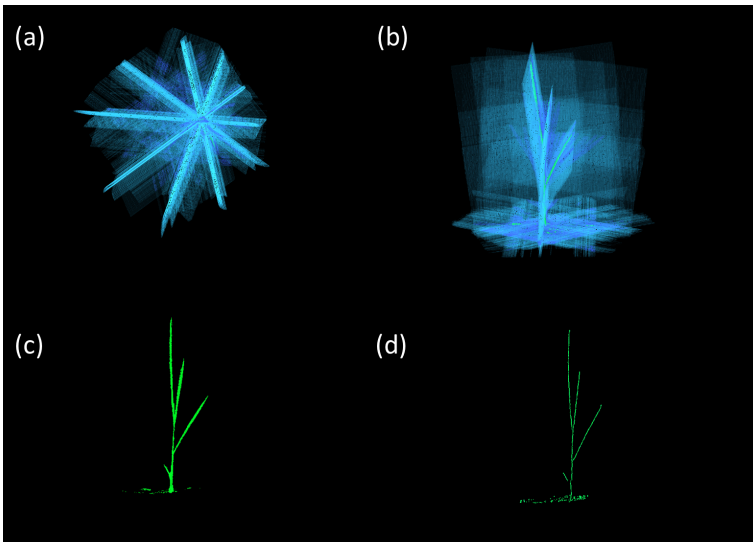

Figure 3.4: The 3D reconstruction for rice images. (a) Top view and side view (b) of a backprojection process. (c) 3D visual hull and skeleton/structure (d) of a rice plant.

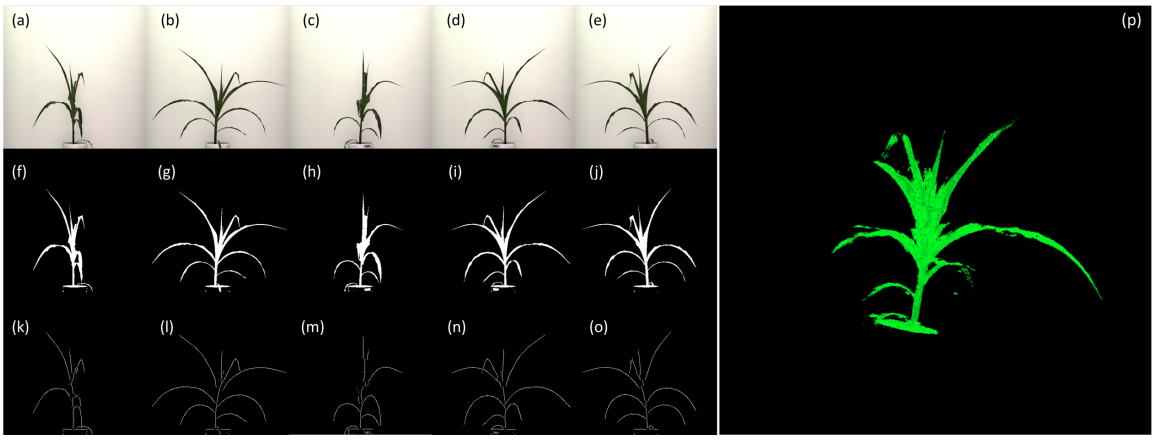

Figure 3.5: The image processing and 3D reconstruction for maize images. (a)-(e) Original input images from different angles. (f)-(j) Silhouette/binary images. (k)-(o) Skeletonized images. (p) 3D visual hull of a maize plant.

extended to other plant image system. Maize plants have relatively complex structures and the results of applying our algorithm to a maize data set are shown in Fig. 3.5. Some leaves in the 3D visual hull of the maize plant are shorter than those of real plants. This is due to the occlusion among leaves and may be solved by taking more images at other angles.

Chapter 4

Hyperspectral Image Information Mining and Visualization

4.1 Volume rendering in hyperspectral images

As it has been discussed in Chapter 2, the stacking of hyperspectral images along the λ direction leads to a hyperspectral data cube and it is worth developing a novel 3D interactive tool allowing users to explore this data cube and obtain information in the 2D image and the 1D spectral simultaneously. For a given spectral feature, users want to know the spatial information where the feature shows up and for a given spatial location, users are interested in learning the spectral information. To achieve this, we are inspired by existing volume rendering techniques that have been proposed to intuitively visualize complex structure within volumetric data. For example, the transfer functions (TF) can be used to assign opacity, color and emittance. The hyperspectral data cube is also in 3D volume data format containing scalar data value. At a given 3D data point/voxel (x, y, λ), namely, a pixel (x, y) and a band λ, there is one intensity value associated. It seems that existent transfer function techniques for volume data in computer graphic field may be adapted directly to visualize

hyperspectral data cubes and explore interesting structures.

However, hyperspectral data cubes have differences from traditional volumetric data sets. In a hyperspectral data cube, the third dimension λ should be considered individually. The projection on the $X-Y$ plane gives spatial information but the projection on $X-\lambda$ or $X-\lambda$ plane is less intuitive since it mixes the spatial space and the spectral or phase space. For a 3D object in the traditional volume, the interior region of this object has a relatively constant value. The boundaries exist as a 3D surface enclosing the object. For an object in the hyperspectral cube, the boundaries that exist in the $X-Y$ plane correspond to the actual boundaries of the object, and ideally these boundaries will be reserved along the entire λ range. However, the boundaries in the λ dimension is not the real boundaries of objects but the spectral patterns. Many research efforts have been devoted to transfer function designs [20, 1]. The traditional usage of transfer functions for volume rendering is still comparably limited to identifying important features in a hyperspectral cube, as there is a lack of transfer functions that are designed to treat the variable variation in one direction particularly. In a hyperspectral cube, the intensity variation along the λ direction, namely the spectral information, characterizes the different substances. The traditional transfer functions used in volume classification cannot make use of the spectral information. As a result, it leads to incorrect object identification.

4.2 Objectives and our contributions

The hyperspectral images give *absorption* or *reflection* information about different materials interacting with light. In the following parts of the paper, we will use *interaction* to stand for both absorption and reflection that characterize or identify the materials from each other. Then the most important question scientists would like to know from hyperspectral images is that at which band/wavelength the interaction between some regions of interest

(ROI) and light is largest. In other words, the main objectives of studying hyperspectral images can be summarized as following:

- First, explore and identify bands to see which bands are more important among all the bands.
- Second, explore and identify ROIs in the given band ranges. The ROIs are clustered due to the spectra characteristic.

We want to achieve the two objectives in 3D hyperspectral data cube by utilizing volume rendering techniques with a well-designed transfer function. The current existing methods of looking for a transfer function that matches the characteristics of objects in the volume may not be an appropriate solution due to the intrinsic differences between the hyperspectral cube and the traditional volume discussed above. A new transfer function is needed which can extract meaningful information from the cube and treat the λ dimension specifically.

In our work, we present the following technical contributions for developing a real-time interactive tool to explore the hyperspectral data cube by volume rendering.

- We propose a new data model to describe the hyperspectral data cube which contains objects in right prism shapes. Our model is not limited to traditional hyperspectral imaging and can be naturally extended to image sequences. We show three case study including the application of this model to both traditional or extended hyperspectral images: plant science hyperspectral images, physics photoemission electron microscopy (PEEM) images and remote sensing hyperspectral images.
- We derive the correlation between the intensity change of substances in hyperspectral images and the entropy of images. Based on the entropy and information theory, we propose new methods for designing a universal transfer function for hyperspectral

data cubes. Our information metric based transfer function design not only allows users to study the hyperspectral data cube and obtain the spectral and spatial information simultaneously, but also guides unsophisticated users to explore the hyperspectral data cube. In addition, any volumetric data within our data model can use our transfer function for volume rendering and obtain information sensitive rendering results.

- We propose a fast clustering algorithm which is used to group the same substances in a hyperspectral cube. The clustering results help users to identify the same substances in one or more user selected spectral ranges and the clustering results can be refined dynamically by users.

4.3 Rational

4.3.1 The data model of objects in a 3D hyperspectral cube

The formal 3D hyperspectral cube data model is given in this section and illustrated by a synthetic data set. The synthetic data set is a simulated hyperspectral image taken at different bands. There are total 100 images and some of them are picked shown in Fig. 4.1. The substances in the image sequences may or may not shown at some bands due to the different interaction characteristic with light which is quite common in hyperspectral images. The traditional hyperspectral image analysis techniques leverage image fusion to reduce a 3D cube to a 2D image and try to maximize the information shown in the 2D image. The three substances in our example are shown in a 2D fused image. The further clustering information can be obtained from spectra where the three unique spectra from corresponding substances indicating there are three materials. Combining two separated studies of image and spectrum, one can finally identify all the substances. This is the traditional approach

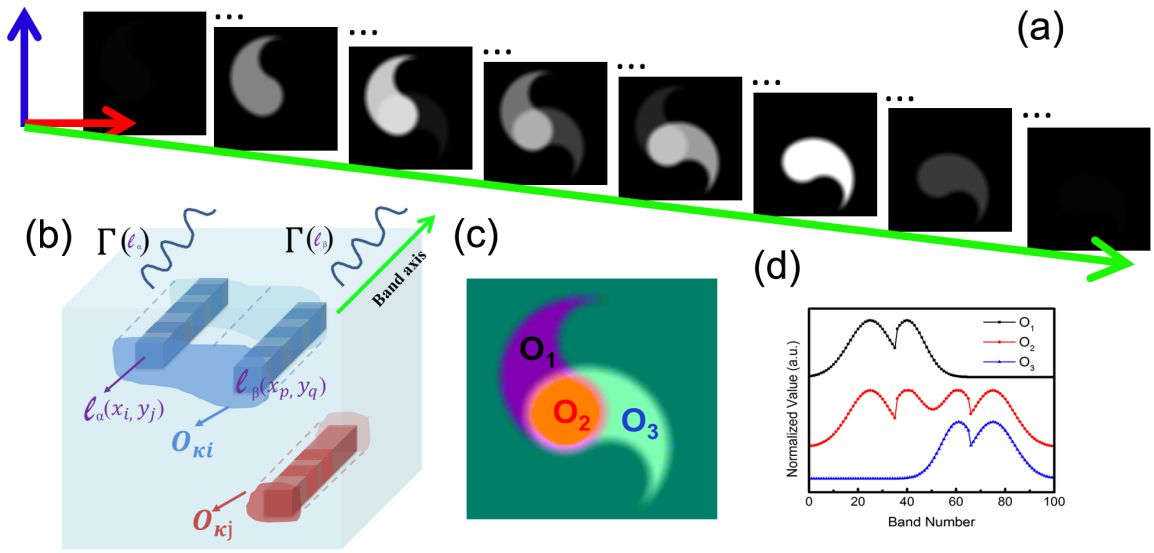

Figure 4.1: The selected images from a synthetic data set are shown in (a). The data model of stacking these image sequences is schematically illustrated in (b). O_{ki} and O_{kj} stand for two different substances and the voxel unions $\ell_\alpha(x_i, y_j))$ and $\ell_\beta(x_i, y_j))$ are assigned to O_{ki} since the spectrum of $\Gamma(\ell_\alpha(x_i, y_j))$ and $\Gamma(\ell_\beta(x_i, y_j))$ are identical. The band direction is indicated by the green arrow. Three substances O_1, O_2 and O_3 exist in the synthetic data set. The boundary between O_1 and O_2 are not shown in the first few images. At the middle range of the bands, three substances are clearly distinguished. At the end of bands, the O_1 is disappearing and the boundary between O_2 and O_3 is merged. (c) shows an image fusion result by PCA indicating 3 substances and (d) gives the spectral properties of three substances.

as introduced in Section 2. By using traditional 3D volume rendering techniques, we can obtain a 3D cube. We can abstract the data model and formally define it. Later we show, within the frame of our data model, how we can obtain the optimized transfer function and volume rendering results to display the spatial and spectral information in our interactive user interface.

Assume an image $\Phi(\lambda)$ with size $x_m \times y_n = N$ pixels is a 2D image taken at band λ and there are total v bands. The 3D hyperspectral data cube is defined as:

$$\Omega(v) = \{\Phi(\lambda) \mid \lambda = 1, \cdots, v\} \tag{4.1}$$

Each pixel (x,y) in an image $\Phi(\lambda)$ for $\lambda \in \{1,\cdots,v\}$ shows up v times in a 3D hyperspectral cube. The order of stacking $\Phi(\lambda)$ to 3D cube is essential and usually in increment order and then for each given pixel $(x_i,y_j) \in \{(x,y) \mid x \in x_m, y \in y_n\}$ it gives a ordered voxel union $\ell_v(x_i,y_j) = \bigcup_{\lambda=1}^{v} (x_i,y_j,\lambda)$ in the 3D space. For a given voxel (x_i,y_j,λ_k) in a 3D hyperspectral cube, there is an intensity value associated with the voxel. The plot of these intensity values associated with a voxel union $\ell_v(x_i,y_j)$ versus $\lambda \in [1,v]$ is referred as a spectrum for $\ell_v(x_i,y_j)$ within a selected band range v and labeled as $\Gamma(\ell_v(x_i,y_j))$.

The ordered voxel unions are clustered together under some distance metric measurement for the spectra associated with the unions. For example, the plot of $\Gamma(\ell)$ *vs* λ for synthetic data set gives spectra/curves as shown in Fig. 4.1 (c) and the similar analysis among curves can be used for clustering and this is usually performed by domain experts. The $\ell(x_i,y_j)$ union is assigned to one and only one substance O_κ implying $O_\kappa \cap O_{\kappa'} = \emptyset$ for $\kappa \neq \kappa'$, where the substance O_κ is defined as:

$$O_\kappa = \{\ell_\alpha(x_i,y_j) \mid metric(\Gamma(\ell_\alpha(x_i,y_j))) < \varepsilon, \alpha \in [1,N]\} \tag{4.2}$$

where $metric(\Gamma(\ell_\alpha(x_i,y_j))) < \varepsilon$ means a spectrum $\Gamma(\ell_\alpha(x_i,y_j))$ satisfies some user-defined metric measurement, and then the different $\ell_\alpha(x_i,y_j)$ are grouped into different groups. The user-defined metric usually measures the spectrum characteristics of voxel unions. The total number of $\ell(x_i,y_j)$ is bounded by the image size N.

The physical meaning of substance is that in the hyperspectral 3D cube, there are many materials which are mapped to the image $\Phi(\lambda)$ and then the spectrum $\Gamma(\ell_\alpha(x_i,y_j))$ of a voxel union $\ell(x_i,y_j)$ gives the characteristic of interaction between materials and light. Under the selected metric, one can eventually identify and cluster the same material and group the voxel unions corresponding to each material together. The grouped voxel unions in 3D cube are from the same material in our 3D cube model. We confine the discussion

of the data model in ideal hyperspectral imaging condition which means the objects are mapped to corresponding pixels in $\Phi(\lambda)$. In reality, the linear or non-linear mixture of spectral characteristics [33] happens, causing mapping of the spectral information from one or more objects from the real world into the same pixels in $\Phi(\lambda)$. As a result, the pixels in $\Phi(\lambda)$ corresponding to the boundary of two materials in the real world are mapped with the spectral information for both materials. This may introduce an artificial substance at the boundary since the superposition changes its spectral characteristic. Other camera related imaging conditions (such as chromatic aberration and/or spherical aberration) with the spectral mixture contribute to forming different substances with blurred boundaries in $\Phi(\lambda)$. However, our 3D data model is still valid in these conditions and we only need to consider the resolved artificial substances as ordinary substances in a 3D cube.

From the discussion above, in the hyperspectral data cube of the entire range, we have the following equation holds whether it is in ideal or non-ideal image condition:

$$\Omega(v) = \bigcup_{\kappa=1}^{s(v)} O_{\kappa}(v) \tag{4.3}$$

where $s(v)$ is the total number of substances depending on v.

From the topology point of view, each and every voxel union $\ell_{\alpha}(x_i, y_j) \in O_{\kappa}$ may or may not be connected to each other. Since the voxel unions are obtained by stacking pixels $(x_i, y_j) \in \Phi(\lambda)$ along λ direction, if the connected pixels (x_i, y_j) form congruent polygons then the corresponding voxel unions $\ell_{\alpha}(x_i, y_j)$ are connected and form prism shapes in a 3D hypercube. It is straightforward to know the prism is a right prism from the stacking direction which is orthogonal to the image plane. Each O_{κ} can approximately be described as a union of right prism shapes. These right prism may or may not be connected.

An important fact in hyperspectral data cube model is that the total substances number depends on the selected band range. If we select a band range resulting sub-total $\mu < v$

bands, then eq. 4.1 and eq. 4.3 become:

$$\Omega(\mu) = \{\Phi(\lambda) \mid \lambda = i, \cdots, \mu + i - 1\} = \bigcup_{\kappa=1}^{s(\mu)} O_\kappa(\mu) \tag{4.4}$$

For a given voxel union $\ell_g(x_i, y_j)$, $g \in [1, N]$ clustering to the substance s_t, $\ell_g(x_i, y_j) \subset O_{\kappa=s_t}(v)$ in the entire band range v, it may be clustered to another substance when partial bands are selected giving $\ell_g(x_i, y_j) \subset O_{\kappa=s'_t}(\mu)$. As shown in the image sequences in Fig. 4.1, the substances O_1 and O_2 are not distinguishable at the front of the band range. If we only select these regions then O_1 and O_2 are clustered as a superset O'_{12} cluster. More discussions are shown in Section 4.4 by the synthetic data set.

Generally, we obtain the important facts with respect to band selection in a hyperspectral cube for $\mu < v$:

$$O_{\kappa=s_t}(v) \subset O_{\kappa=s'_t}(\mu) \tag{4.5}$$

If we project $\Omega(u)$ for a given u along λ direction and map the same $O_\kappa(u) \in \Omega(u)$ to a 2D image with the same attribute (*i.e.* intensity or color), we can get a substances map Φ_u corresponding to selected band range u. For example, in our synthetic data set, if only first few bands are selected, then the substance map only contains the union of O_1 and O_2 since the spectral information of O_1 and O_2 is identical in the selected band ranges. All the existing image fusion results are equivalent to obtain a substances map Φ_u.

Since $O_\kappa(\mu <= v)$ may be known (supervised) or not (unsupervised) and it strongly depends on the selected sub-band ranges, the band selection and dynamically changed O_κ are desired for the tools for studying the hyperspectral data cube.

Our data model of hyperspectral 3D cube indicates the significant difference from traditional 3D volumetric data. In traditional 3D cube, objects can be distinguished from boundaries and within a given boundary. The density values of a object are relatively ho-

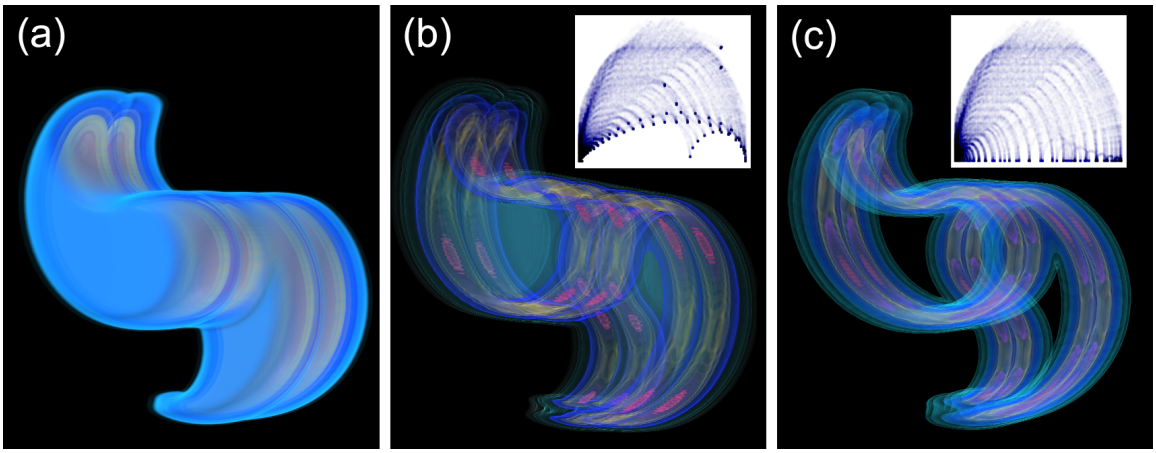

Figure 4.2: The stacking of 2D images from synthetic data set to a 3D hyperspectral cube. The intensity based transfer function and volume rendering results are in the left panel. The middle and right one are corresponding to gradient based transfer function and the volume rendering results are shown for 3D gradient and 2D gradient (in image plane only) respectively.

mogeneous and the shape of object is arbitrary. If we use the volume rendering techniques for traditional 3D volumes, the substance in hyperspectral 3D cube will be misleadingly divided from the λ direction, making the rendering results meaningless. For example, the synthetic data set is shown in Fig. 4.2 (a) by volume rendering. The volume rendering summarizes all the image sequences information in one volume. The information in the 3D cube is very compacted and the 3D cube is more feasible to mining information than hundreds of images. This is the advantage of volume rendering. However, the three substances are not directly segmented due to the intensity based transfer functions used in volume rendering. If the intensities of two voxels are same, the same opacity or color is assigned to make the voxels indistinguishable. In the hyperspectral cube, it is not the intensities but the spectra or the intensity union along a series of voxels (locality) determining what color or opacity the voxels should be assigned. The gradient based transfer function [20] seems to make use of the locality information of an intensity with the neighbors since the intensity gradient is calculated from the neighbor pixels. Unfortunately, the 3D gradient of

a hyperspectral cube is less intuitive since the 3D gradient mixes the spectral and spatial information. Fig. 4.2 (b) shows the 3D gradient transfer function and the volume rendering results. The edges are detected but they divide the substances in the band direction, which is incorrect. The 3D hyperspectral cube is formed by stacking 2D images. Compared with the 3D gradient transfer function, the 2D gradient only calculates the spatial information in a given image and then has a meaningful explanation. As shown in Fig. 4.2 (c), a 2D gradient transfer function identifies all the edges in the images. However, the three substances shown in Fig. 4.1 (c) is hard to be detected by the gradient based transfer function.

We need to design a new type transfer function for hyperspectral 3D data cube in order to achieve two objectives described in section 4.2. The first objective studies the spectral character and the second studies the spatial character of hyperspectral images. The change of the interaction indicates the importance of a band. This can be illustrated by the change of intensity of a region in hyperspectral images. Similarly, at a given band, scientists would like to know which regions in the image are changing with respect to intensity. The same materials will give the same interaction patterns and therefore the clustering can be achieved by analyzing the interaction patterns with light in given band range. As we introduced in a previous section, traditionally the two main objectives are studied individually. In our approach, once we consider the hyperspectral images as a 3D data cube, we can study the spectral and spatial characters simultaneously by designing a transfer function for the hyperspectral data cube so that the volume rendering techniques provides us an interactive tool to explore the 3D data cube. In addition, the real-time interaction is necessary and then scientists can use the transfer function explore and learn all the important information simultaneously and instantly in spatial and spectral space.

4.3.2 Entropy

The 3D hyperspectral data cube is constructed by stacking images taken at each band. The entropy for each image can be calculated based on Shannon's entropy. By assuming each pixel in an image is an independent and identically distributed realization, we can obtain the probability of a intensity value in an image from the intensity histogram plot of the image. For an image with $x_m \times y_n = N$ total pixels, h_i denotes the histogram entry of intensity value i and the probability of pixel intensity is $p_i = h_i/N$. Under this model, the entropy of an image is defined as:

$$H = -\sum_i p_i \times log(p_i) \tag{4.6}$$

From the image entropy definition, it is clear to see only the distribution of intensity namely the histogram will affect the value of entropy. The intensity variation is reflected by entropy which has larger tolerance to noise and other extrinsic imaging conditions. For example, if the distribution remains the same but the total intensity change due to exposure time will not change the entropy. A noise pixel, pixel shift or object drifting during imaging will give limited change in entropy which is negligible.

In the hyperspectral images, if the absorption of light happens then the intensity of image will change accordingly. As a result, the distributions of intensity changes. At one band λ_δ, the average intensity I of hyperspectral image $\Phi(\lambda_\delta)$ is described by the following equation:

$$I = \frac{C_0 I_0 + C_1 I_1 + \cdots + C_i I_i + \cdots + C_j I_j + \cdots + C_n I_n}{\sum_k C_k} \tag{4.7}$$

where $\{I_0, \cdots, I_n\}$ are all possible intensity value sample space and n is the total discretized intensity value (*e.g.* n is typically chosen to be 255 for an 8-bit gray image.); $C_k \in \{0, \cdots, N\}$ is the total count of the corresponding intensity where $N = x_m \times y_n$ is the total pixels the x_m by y_n image contains and C_k is constrained by the total pixels of the

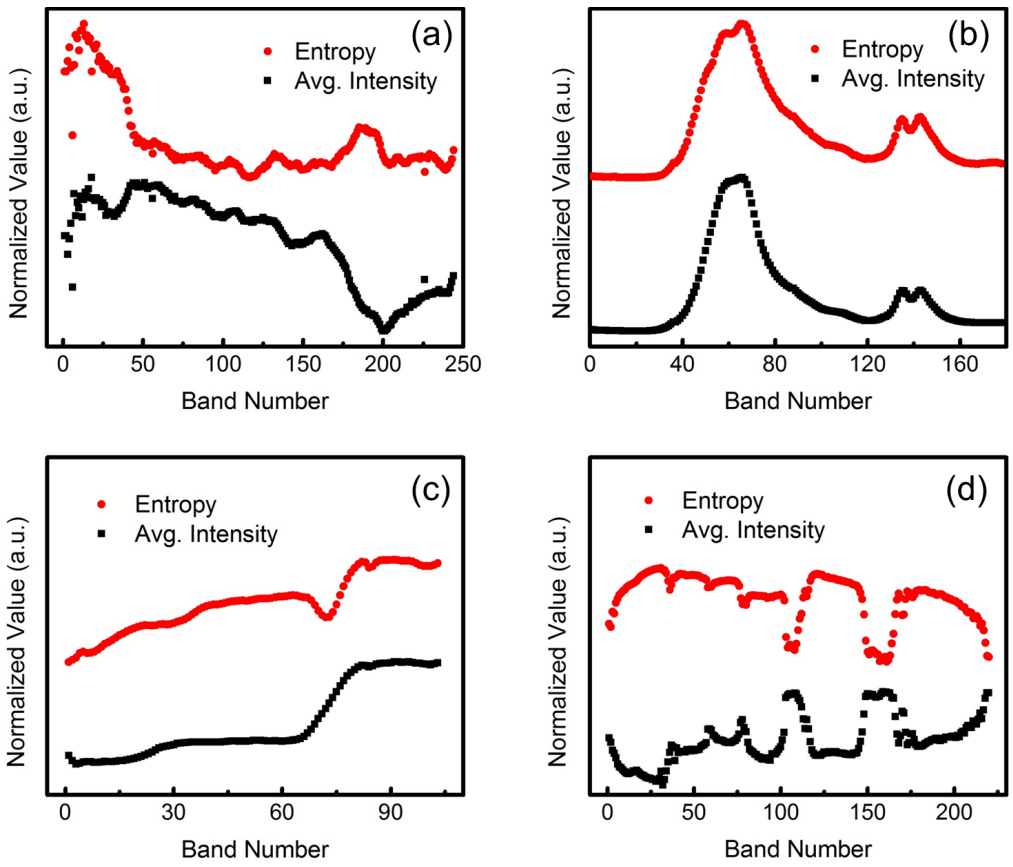

Figure 4.3: The average intensity and entropy plots for images across the entire bands. Four sets of hyperspectral images from three different scientific fields including (a) plant science, (b) physics, and (c)-(d) remote sensing are used to show the generalization of the correlation between image intensity and entropy.

image implying $\sum_{k=0}^{n} C_k = N$.

From the equation 4.7, we can get the probability P of an intensity value I_α in the image as:

$$P_{I_\alpha} = \frac{C_\alpha}{\sum_{k=0}^{n} C_k} = \frac{C_\alpha}{N} \tag{4.8}$$

The entropy of image $\Phi(\lambda_\delta)$ based on equation 4.6 is given by:

$$\begin{aligned} H(\lambda_\delta) &= -\sum_{\alpha=0}^{n} P_{I_\alpha} log(P_{I_\alpha}) \\ &= -\sum_{\beta \notin i,j} P_{I_\beta} log(P_{I_\beta}) - P_{I_i} log(P_{I_i}) - P_{I_j} log(P_{I_j}) \end{aligned} \tag{4.9}$$

If the count of an arbitrary intensity I_i changes to $I_j \in \{I_0, \cdots, I_n\}$ then the P_{I_i} and P_{I_j} will change accordingly and the entropy value in the equation above may be altered. Assume there are originally Δ_c pixels with intensity I_i defined as a ROI in $\Phi(\lambda_\delta)$, and due to the interaction with lights at another band $\lambda_{\delta'}$ the original intensity I_i changes to intensity I_j. In image $\Phi(\lambda_\delta)$, the initial counts of I_i and I_j are C_i and C_j respectively. Then in image $\Phi(\lambda_{\delta'})$ the counts C'_i and C'_j for I_i and I_j change to $C'_i = C_i - \Delta_c$ and $C'_j = C_j + \Delta_c$. The probabilities P'_{I_i} and P'_{I_j} also changed to $P'_{I_i} = \frac{C_i - \Delta_c}{N}$ and $P'_{I_j} = \frac{C_j + \Delta_c}{N}$

The entropy of image $\Phi(\lambda_{\delta'})$ taken at band $\lambda_{\delta'}$ changes accordingly

$$H(\lambda_{\delta'}) = -\sum_{\beta \notin i,j} P_{I_\beta} log(P_{I_\beta}) - P'_{I_i} log(P'_{I_i}) - P'_{I_j} log(P'_{I_j}) \tag{4.10}$$

Combining eq. 4.9 and 4.10, we get the entropy change due to intensity change:

$$\begin{aligned} \Delta H_{\lambda_\delta - \lambda_{\delta'}} &= \Delta(H(\lambda_\delta) - H(\lambda_{\delta'})) \\ &= P'_{I_i} log(P'_{I_i}) + P'_{I_j} log(P'_{I_j}) - P_{I_i} log(P_{I_i}) - P_{I_j} log(P_{I_j}) \end{aligned} \tag{4.11}$$

In the scenario we discussed above, we assume the intensity did not change dramatically beyond the ROI so in eq. 4.9 and 4.10 the first term remains the same. This assumption is valid due to the fact how the light interacts with matters, namely if the photon energies mismatch the energy band gap of the materials, the transmission/absorption rate is independent the energies. When the photon energy lines around the energy band gap of materials, the transmission/absorption rate depends on the energy. One can always find the bands with a

large intensity change for a selected ROI in an image and the region beyond the ROI will not change much among the selected bands.

Theoretically, eq. 4.11 may equal to zero but in practical, since the hyperspectral bands for imaging is particular chosen by domain scientists for studying the particular materials in the bands, so the intensity change are large across the entire band space and the change of entropy is also noticeable. The hyperspectral image intensity *vs* entropy plot is shown in Fig. 4.3 from different scientific fields, which confirms the correlation between entropy change and average intensity variety of an image.

The intensity change of an image reflects the interaction between materials with lights which is the keystone for studying hyperspectral images. Although intensity plays a key role in interpreting the hyperspectral images, it is subjected to some vital defects. The image intensity depends on the experimental environments. For example, the exposure time, thermal fluctuation of charge-coupled device (CCD) and noises may be different for images taken at different bands which make the direct intensity comparison meaningless. The intensity is assigned to each and every voxel in 3D data cube and it only gives local information. The voxel-by-voxel intensity analysis is subject to noise and not feasible. In order to overcome these difficulties, we will make use of entropy of an image. In our transfer function design, we keep the entropy *vs* band number plot. Since the intensity change is correlated with entropy as shown in eq. 4.11 one can look for the bands where entropy changes dramatically.

The first objective namely identifies the important bands can be achieved by making use of entropy *vs* band number plot. Once we select a band range u or many discrete band ranges, the next objective is identifying the ROIs or substances $O_{\kappa}(u) \in \Omega(u)$ in the contiguous or non-contiguous given band ranges by clustering voxel unions as eq. 4.1 shown. One metric is needed to character the spectrum value set $\Gamma(\ell_v(x_i, y_j))$ associated with a voxel union $\ell_v(x_i, y_j)$ for further clustering the voxel unions to substances. On one

hand, a spectrum set can be interpreted as a set of curves. The similarity between curves can be calculated among curves to identify the characteristics. Usually, the comparison among curves gives $O(N^2)$ time complexity where N is the total number of curves. On the other hand, if the value $\Gamma_{v_i} \in \Gamma(\ell_v(x_i, y_j))$ is considered as a random variable, then we can apply statistical methods to variable set $\{\Gamma_{v_i}\}$ including standard deviation, skewness and so on which evaluate each set $\{\Gamma_{v_i}\}$ individually resulting in $O(N)$ time complexity which is preferable for real-time applications. In the following section, the metric of evaluating set $\{\Gamma_{v_i}\}$ and the clustering based on the metric is given.

4.3.3 Curve evaluation metric

Skewness is a measure to evaluate how asymmetric the distribution of a given set of values. If distribution is symmetric the skewness of it is zero. Asymmetric distribution gives either positive value or negative value. For a given random variable sample set $\{x_i\}$ with mean of $\bar{x}$ and standard deviation $\sigma_x = \sqrt{\frac{1}{N}\sum_{i=1}^{N}(x_i - \bar{x})^2}$ the skewness S is defined as:

$$S = \frac{\frac{1}{N}\sum_{i=1}^{N}(x_i - \bar{x})^3}{(\frac{1}{N}\sum_{i=1}^{N}(x_i - \bar{x})^2)^{\frac{3}{2}}} = \frac{\frac{1}{N}\sum_{i=1}^{N}(x_i - \bar{x})^3}{\sigma_x^3} \tag{4.12}$$

In a given band range $u \in [1, v]$, there are total N spectrum set $\Gamma(\ell_u(x_i, y_j))$. We propose a formula inspired by skewness calculation to characterizes the spectrum value set $\{\Gamma_{u_\delta}\}$ associated with a voxel union $\ell_u(x_i, y_j)$. We define the curve-skewness ς of a given spectrum value set $\{\Gamma_{u_\delta}\}$ as

$$\varsigma = \frac{\frac{1}{\sum_{\delta=1}^{u}\Gamma_{u_\delta}} \times \sum_{\delta=1}^{u}[\Gamma_{u_\delta} \times (\delta - \zeta)^3]}{(\frac{1}{\sum_{\delta=1}^{u}\Gamma_{u_\delta}} \times \sum_{\delta=1}^{u}[\Gamma_{u_\delta} \times (\delta - \zeta)^2])^{\frac{3}{2}}} \tag{4.13}$$

where

$$\zeta = \sum_{\delta=1}^{u} (\Gamma_{u_\delta} \times \delta) / \sum_{\delta=1}^{u} \Gamma_{u_\delta}$$

For each voxel union $\ell_{u_\delta}(x_i, y_j) \in \Omega(u)$ we can evaluate the corresponding spectrum value set $\{\Gamma_{u_\delta}\}$ by eq. 4.13 to calculate the curve-skewness score. All the curve-skewness scores for voxel unions $\ell_u(x_i, y_j)$ where $x_i \in x_m$ and $y_j \in y_n$ consist a matrix Ψ_u with dimension x_m and y_n. Every point in matrix Ψ_u corresponds to a spectrum characteristic in a hyperspectral 3D cube in given band range u. If the values shown in matrix Ψ_u are clustering then it is equivalent to cluster the corresponding voxel unions $\ell_u(x_i, y_j)$.

The physical reason that one can use curve-skewness score to identify a spectrum corresponding to a voxel union $\ell_{u_\delta}(x_i, y_j)$ is that the interaction with light results a peak/valley in the spectrum point of view. In a given range of bands, the shape of peaks/valleys identifies the materials so the curve-skewness score ς represents the shape/asymmetric character of a spectrum resulting from the interaction between light and the materials. In order to achieve the second objective in exploring a 3D hyperspectral cube namely identify and cluster the ROIs, the clustering of points in matrix Ψ_u based on their values is used. Since the comparable spectra gives similar curve-skewness scores identifying the similar interaction with lights, we just divide all the values in matrix Ψ_u into different bins based on the value ranges which essentially is the histogram of values of matrix Ψ_u. For the same bin, we can map the values back to the spectra associated with different voxel unions and cluster the voxel unions in one group. The average of spectra in the same bin represents the spectral information of voxels in 3D hyperspectral cube. Given the 3D cube $\Omega(u)$, our procedure is summarized in the following algorithm which calculates the spectra properties in given band range u and the clustering in $\Omega(u)$ is achieved.

In our algorithm , users can define the bin size N_B to explore the 3D hyperspectral cube. The curve-skewness algorithm is applied to our synthetic data set. It shows promising clus-

Algorithm 2 Voxel Union Clustering

Initialize a matrix Ψ_u with size x_m by y_n
Initialize an average spectrum set $\Gamma_{avg} = \{\emptyset\}$
for each voxel union $\ell_{u_\delta}(x_i, y_j) \in \Omega(u)$ **do**
    Get value set $\{\Gamma_{u_\delta}\}$ associated with $\ell_{u_\delta}(x_i, y_j)$
    Get $\varsigma_{i,j}$ for value set $\{\Gamma_{u_\delta}\}$ corresponding to pixel (x_i, y_j) ▷ calculated by eq. 4.13
    Write $\varsigma_{i,j}$ to matrix Ψ_u(i,j)
end for
Define a bin number N_B ▷ User defined N_B
Get the histogram of matrix Ψ_u(i,j) with respect to N_B
for each bin N_{B_i} **do**
    for each value $val \in N_{B_i}$ **do**
        Get the voxel union $\ell_{u_\delta}(x_i, y_j)$ corresponding to val
        Assign $\ell_{u_\delta}(x_i, y_j)$ into cluster $O_{N_{B_i}}$
    end for
    Get mean spectrum $\Gamma(O_{N_{B_i}})$ for all spectra in cluster $O_{N_{B_i}}$
    Add $\Gamma(O_{N_{B_i}})$ to Γ_{avg}
end for

tering results as shown in Fig. 4.4 (a)-(c). All the three substances are clustering correctly. We also show the case that the selected bands affect the clustering. In the Fig. 4.4 (d) and (f), we only select the first or last few bands and the substances are not distinguishable in these bands. The band selection is critical for identifying instances and hence the entropy guided transfer function is necessary and can help unsophisticated users to explore the 3D hyperspectral cube. In the Fig. 4.4 (e), we show that with a carefully selection of band range the edge of substances can also be detected as an artificial substance. If the boundaries mix the spectral information resulting from a superposition of spectra, our method can also be used to detect object edges.

In Section 4.4, we show how we integrate the algorithm and entropy into our user interface and our real-time interactive design gives the state-of-art visualization tool to study the spectral and spatial information simultaneously by volume rendering.

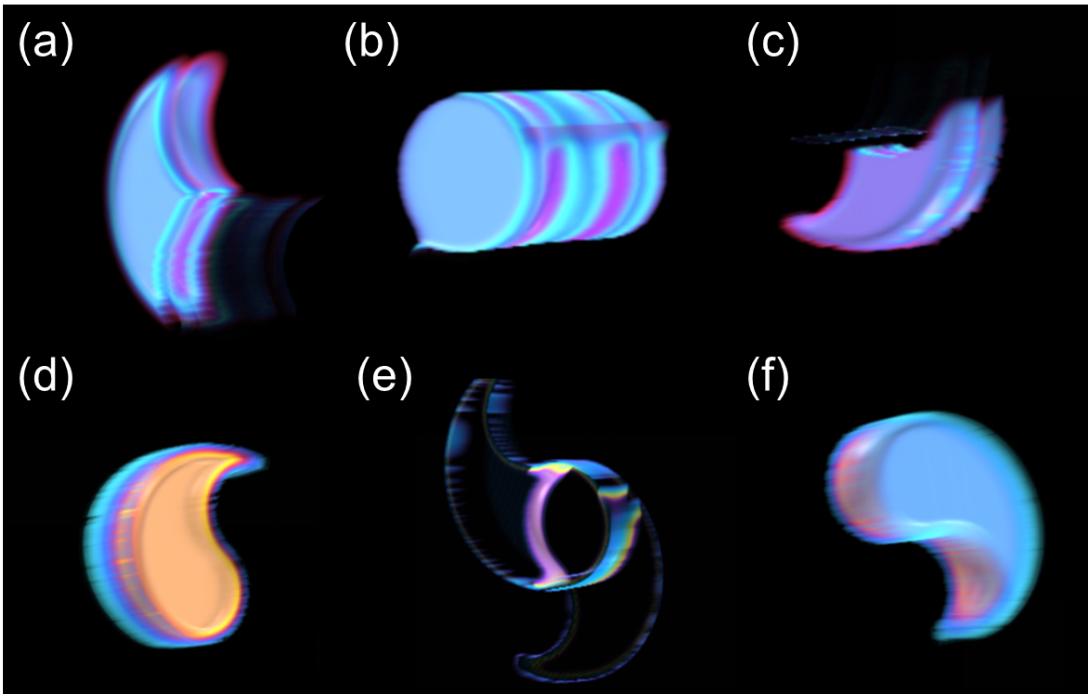

Figure 4.4: The three substances are clustered by our method and interface. The boundaries can also be detected.

4.4 Implementation

In this section, we introduce how we make use of entropy and curve-skewness score to design a transfer function which allows users to explore the hyperspectral 3D data cube. Two interface screenshots with an application in physics PEEM images are shown in Fig. 4.5 indicating the successful segmentation of two structure phases of oxides [7].

The interface contains 5 windows. Window 1 displays the 3D hyperspectral data cube. The program load 2D images stacking along λ direction resulting in a 3D cube which is rendered using intensity based transfer function. User can rotate the cube and zoom in and out to explore it. Once the images are loaded, Window 2 displaying a plot of the entropy vs band number across the entire band range. A hyperspectral image with high entropy is more likely to provide useful information about the substances it contains. This window can guide users to do an unsupervised exploring. Users can select one or multiple ranges.

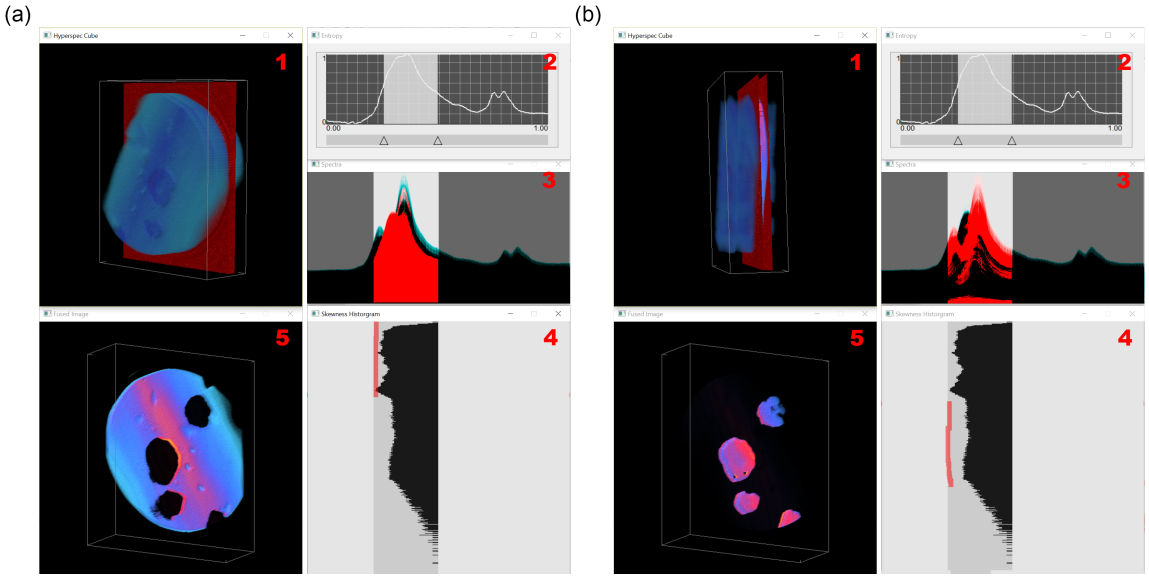

Figure 4.5: The user interface with an application in physics PEEM images

One left click of mouse generates a pair of triangular sliders and by click-and-hold users can slide the sliders to the interested range. Right click on a slide will remove it with the one it was paired with. In our example, one peak envelope of entropy is selected. The dramatical entropy envelope change indicates an importance of these bands as we discussed in section 4.3.2. Once the band range are selected, the volume rendering results in Window 1 will change by showing red planes indicating the selection. The implementation of our curve-skewness algorithm calculates the curve skewness score for the selected band range and return a histogram map shown in Window 4. Windows 4 changes in real-time corresponding to one or more band range selections. The bin number associated with histogram is set to 1024 for physics PEEM data and can be adjusted by users for generating histograms. The averaged spectra for the same bin are shown in Window 3. Since each bin contains corresponding sets of voxel unions, once the bins in the histogram are selected by users, the program highlights the selection in red, and the corresponding voxels are shown in Window 5. At the meantime, the spectra are highlighted in red to indicate the spectral

characters.

The brush of histogram allows users to obtain dynamically changed spectra and spatial information simultaneously. User can select multiple bands at the same time and multiple corresponding histograms are shown. By brushing the different histograms, the unsupervised interactive studies are achieved. Our transfer function designed for hyperspectral data cube utilizes entropy and curve-skewness shown in Window 2 and 4. The spatial and spectral information are dynamically shown in Window 1, 3, and 5. By using our tool, scientists can explore and study the hyperspectral images in both spatial and spectral dimensions. As shown in Fig. 4.5 the different brush positions in histogram give two different phases of oxides. The brush positions highlighted in red in Fig. 4.5 (a) Window 4 are lowered in Fig. 4.5 (b) Window 4. Different bins correspond to different instances indicating the similar voxels are clustering in the bins and confirms the validness of our methods. More discussion of these brush results are shown in section 5.1.

4.5 Case study

4.5.1 Application in physics PEEM image

In this section, we show how the hyperspectral 3D data cube can be explored and studied by our tool in different scientific domains. First, we show an application of our method in physics domain. The X-ray PEEM images are taken with X-ray energy corresponding to Fe absorption edge. The hyperspectral images with size 608×496 of oxide $LuFeO_3$ were taken across 178 band. These images consist a 3D hyperspectral data cube with dimension of $608 \times 496 \times 178$. Two selected images from band 55 and 65 and a PCA fused image are shown in Fig. 4.6. In the image, there are mainly three substances. The trivial substance is the aperture shown as the gray square with a circle in the middle shown in Fig. 4.6.

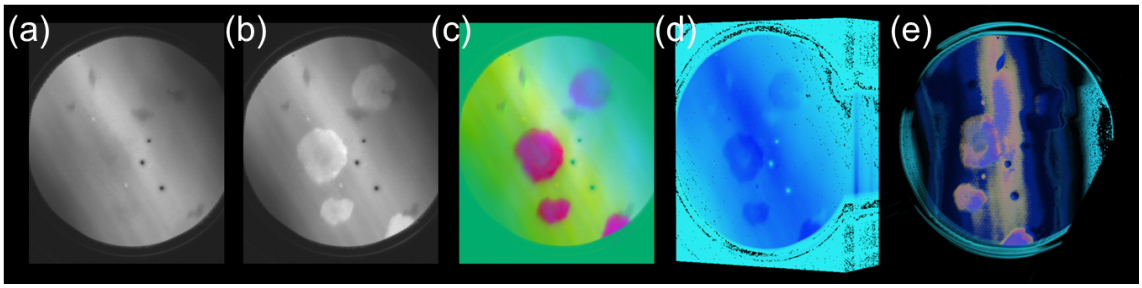

Figure 4.6: Two gray images (a)-(b) from band 55 and 65, a PCA image fusion result (c) with pseudo color, the volume rendering (d) of images in 3D hyperspectral data cube and volume rendering results (e) by intensity based transfer function are shown for physics PEEM data set. There are three black dots corresponding to dead pixels in CCD show in gray images.

Inside the circle there are two important substances which draw physicists interest. One is hexagonal $LuFeO_3$ and another one is orthorhombic $LuFeO_3$ referred as h-LFO and o-LFO respectively. The spatial relation between h-LFO and o-LFO can be considered as o-LFO islands(shown in red in PCA image) sitting on h-LFO background (the rest area inside the circle). The o-LFO is barely noticeable in band 55 but shows as white islands in band 65 indicating the X-ray absorption character. The small darker regions with irregular shape in original images from both bands is the morphology shape giving the contrast as well but actually it is the h-LFO. The strip contrasts are from the X-ray light which has inhomogeneous intensity. The inhomogeneous X-ray introduce the difficulties to distinguish h-LFO and o-LFO as shown in the volume rendering result. However, since h-LFO and o-LFO have different absorption character with respect to X-ray, by our method we can get the islands and background separated as shown in Fig. 4.5. Previously, scientist usually use one individual image to represent the entire image sequences and study the spectra accordingly. In our interface, once the h-LFO and o-LFO are distinguished, the corresponding spectra are shown in Window 3 which shows the spectral information. From the spectra information it is easily to confirm the segmentation is correct. The spectra associated with different oxides are highlighted in user interface and consistent with previous study [7].

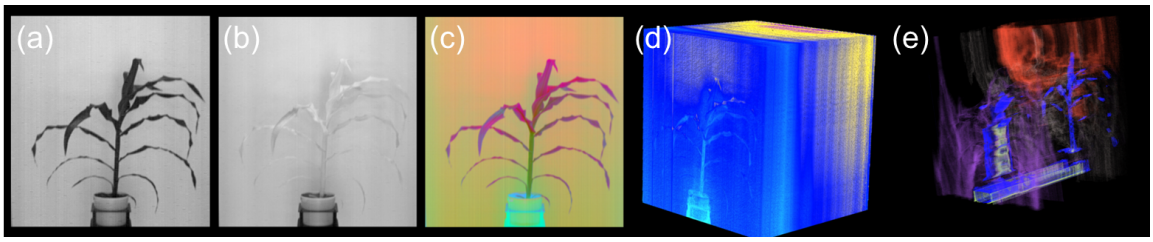

Figure 4.7: Two gray images (a)-(b) from band 27 and 48, a PCA image fusion result (c) with pseudo color, the volume rendering (d) of images in 3D hyperspectral data cube and volume rendering results (e) by intensity based transfer function are shown for maize hyperspectral images.

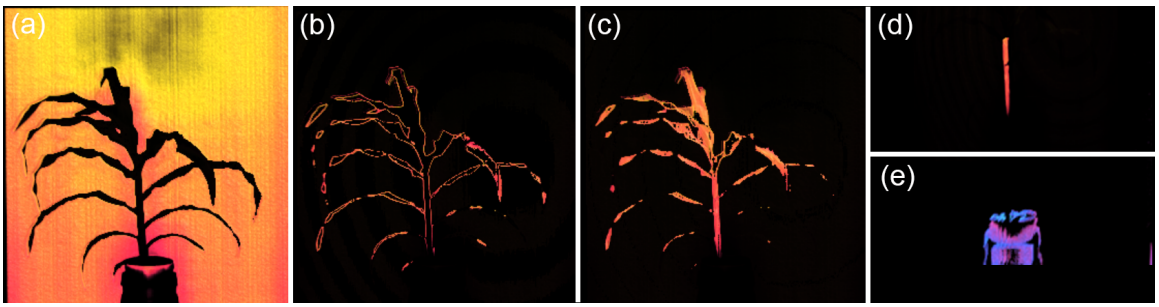

Figure 4.8: The 3D volume rendering results. The segmentation is achieved by our interface. (a) The background. (b) Leaf edges. (c) A maize plant. (d) Stem of a maize and (e) The pot where the maize grows in

4.5.2 Application in plant science

Second, we show an application of our method and user interface in plant science domain. The hyperspectral images with size 261×275 of maize plant were taken across 242 band (from wavelength 545 nm to 1700 nm). These images consist a 3D hyperspectral data cube with dimension of $261 \times 275 \times 244$. Two selected images from band 27 and 48 (corresponding to wavelength 670 nm and 770 nm) and a PCA fused image are shown in Fig. 4.7. From these 2D images, one may identify the plant from the background and pot. The difficulties to identify plants are introduced also by inhomogeneous light intensity. The 3D hyperspectral cube are shown in Fig. 4.7 (d). At most of the band the leaves has same intensity with the background which the plant locates in front of. The intensity based vol-

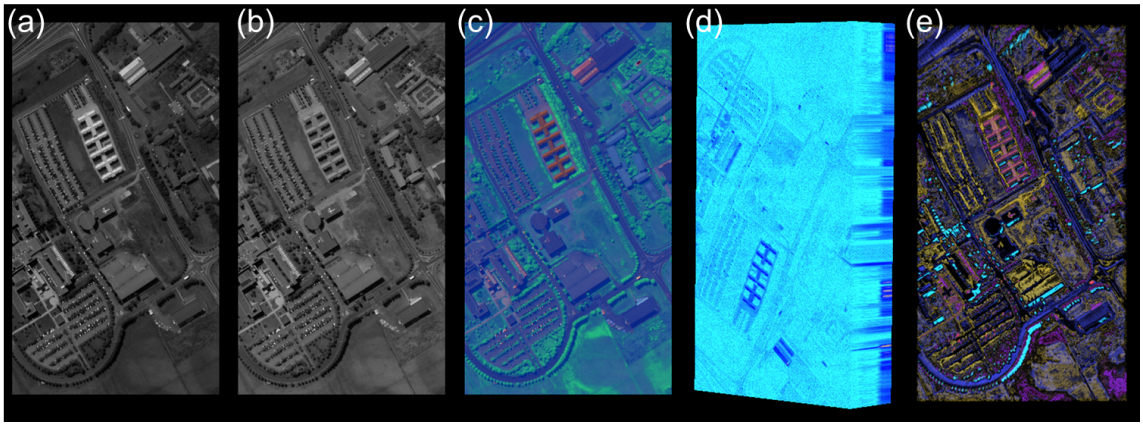

Figure 4.9: Two gray images (a)-(b) from band 30 and 70, a PCA image fusion result (c) with pseudo color, the volume rendering (d) of images in 3D hyperspectral data cube and volume rendering results (e) by intensity based transfer function are shown for Pavia University remote sensing data set

ume rendering results are shown in Fig. 4.7 (e) where the different colors other than blue indicate the complex distribution of background intensity. In this situation, our method still can segment the plant as leaves and stem since the absorption of light for them are different. The background, pot and plat segmentation are shown in Fig. 4.8. Note that the segmentation is done within the volume and it is a 3D segmentation.

In the experimental set-up of the imaging, a white plastic board are used as the background. The white board reflects light and result in a so-called light pollution to plants. Therefore, the edges of plants mix many spectra from different places which distinguishes the edges from others. These boundaries are also detected by our methods shown in Fig. 4.8 (b).

4.5.3 Application in remote sensing

Last but not least, we show an application in remote sensing domain. Reflective Optics System Imaging Spectrometer (ROSIS-03) University of Pavia data is used in this work. The hyperspectral images with size 340×610 were taken across 103 band. These images

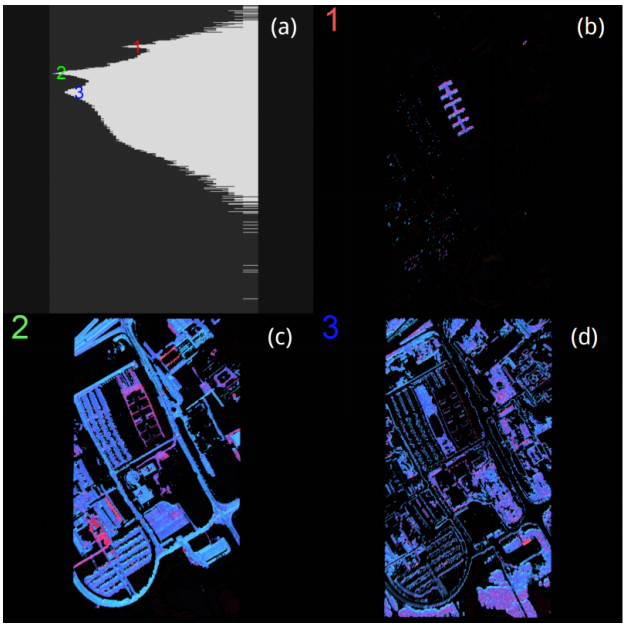

Figure 4.10: Two gray images (a)-(b) from band 30 and 70, a PCA image fusion result (c) with pseudo color, the volume rendering (d) of images in 3D hyperspectral data cube and volume rendering results (e) by intensity based transfer function are shown for Pavia University remote sensing data set

consist a 3D hyperspectral data cube with dimension of $496 \times 608 \times 178$. Two selected images from band 30 and 70 and a PCA fused image are shown in Fig. 4.9. The remote sensing hyperspectral data set has significant difference from the physics and plant data set. In physics or plant data set, the substances within an image usually has limited number. The effective pixels of one substance defined as the pixel count of one substance to the total pixels an image has is large. The experimental environment is control by scientist and the date set are taken in a laboratory. However the remote sensing images may have many unknown or uninterested substances. For example, in the Pavia data set or other remote sensing data set, even in the ground truth there are unclassified area. In addition, the cloud or other uncontrollable noises may also exist. The volume rendering technique in our method can detect some of the materials shown in Fig. 4.10.

Chapter 5

Conclusion and Future Work

In this thesis, we study RGB images and hyperspectral images and present different approaches leading to efficient information mining procedures for these images. The image processing and 3D volume reconstruction techniques for crop plants have been applied to RGB images. We propose an ad-hoc solution for processing a massive amount of image data and obtaining growth information. Our method only needs 5 images from different view angles to reconstruct a visual hull and the structure of a simple plant such as a rice plant. For a complex plant, such as maize, our 2D binarization method also gives promising outputs. However, more images are necessary to obtain an accurate structure. Plant scientists control the growth conditions, such as stress level or light time for different plants, and our approach can tell the differences between plants in different growth conditions for phenotyping studies. The growth information can be subtracted from the reconstructed 3D structures. In the future, we would like to extend the existing segmentation algorithms (such as, region growing) on 3D reconstructions, and enable detailed comparisons between the structures of leaves or stems of different plants.

In order to obtain other information for plant growth, hyperspectral images are taken. Our scopes are not limited to analyzing the hyperspectral images from plants. Instead,

we extend our study to different scientific fields where hyperspectral images are used. In our work, volume rendering technique is introduced first to study the hyperspectral image sequences knows as 3D hyperspectral cube. We develop a real-time interactive tool for explore the 3D cube. Since the 3D hyperspectral cube mixes the spatial and spectra dimensions, the traditional transfer functions such as gradient based transfer function suffer some difficulties to reserve the spectral information and identify substances in 3D cube by making use of spectral information. We formally define a data model for hyperspectral data cube and propose a new method to design a transfer function based on entropy and spectra information. We analyze the significant role the image entropy plays in hyperspectral image sequences and derive the strong correlation between image intensity and entropy. Entropy is a metric that has been widely used to select useful images for image fusion. In the traditional image fusion methods, each image is treated as an individual dimension without considering the relationship between images. However one hyperspectral image is usually highly correlated to its neighboring images in a specific band range. Once one or more important bands are identified, other metrics can be introduced to cluster the substances in the 3D hyperspectral data cube. In this work, we propose a fast $O(N)$ time complexity algorithm calculating a curve-skewness score, where N is the total pixels in one hyperspectral image. The identification of different substances are achieved by calculating curve-skewness scores and this method shows promising results in wide scientific fields including plant science, physics and remote sensing.

Our work gives the initial attempts to build a bridge connecting 3D hyperspectral cubes and volume rendering. In addition, our transfer function and design strategies can be generalized to traditional volumetric data if the data shares some common features with our hyperspectral data model.

Bibliography

[1] A. Ashikhmin, G. Kramer, and S. ten Brink. Extrinsic information transfer functions: model and erasure channel properties. *IEEE Transactions on Information Theory*, 50(11):2657–2673, 2004.

[2] E. Bauer, M. Mundschau, W. Swiech, and W. Telieps. Surface studies by low-energy electron microscopy (LEEM) and conventional UV photoemission electron microscopy (PEEM). *Ultramicroscopy*, 31(1):49–57, 1989.

[3] E. Bauriegel and W. B. Herppich. Hyperspectral and chlorophyll fluorescence imaging for early detection of plant diseases, with special reference to fusarium spec. infections on wheat. *Agriculture*, 4(1):32–57, 2014.

[4] J. M. Bioucas-Dias, A. Plaza, G. Camps-Valls, P. Scheunders, N. Nasrabadi, and J. Chanussot. Hyperspectral remote sensing data analysis and future challenges. *IEEE Geoscience and remote sensing magazine*, 1(2):6–36, 2013.

[5] B. Biskup, H. Scharr, A. Fischbach, A. Wiese-Klinkenberg, U. Schurr, and A. Walter. Diel growth cycle of isolated leaf discs analyzed with a novel, high-throughput three-dimensional imaging method is identical to that of intact leaves. *Plant physiology*, 149(3):1452–1461, 2009.

[6] J. Cai and S. Miklavcic. Automated extraction of three-dimensional cereal plant structures from two-dimensional orthographic images. *IET Image Processing*, 6(6):687–696, 2012.

[7] S. Cao, X. Zhang, K. Sinha, W. Wang, J. Wang, P. A. Dowben, and X. Xu. Phase separation in $LuFeO_3$ films. *Applied Physics Letters*, 108(20):202903, 2016.

[8] C.-G. Chern, M.-J. Fan, S.-M. Yu, A.-L. Hour, P.-C. Lu, Y.-C. Lin, F.-J. Wei, S.-C. Huang, S. Chen, M.-H. Lai, et al. A rice phenomics study phenotype scoring and seed propagation of a T-DNA insertion-induced rice mutant population. *Plant molecular biology*, 65(4):427–438, 2007.

[9] K.-M. Cheung, S. Baker, and T. Kanade. Shape-from-silhouette across time part I: Theory and algorithms. *International Journal of Computer Vision*, 62(3):221–247, 2005.

[10] R. T. Clark, R. B. MacCurdy, J. K. Jung, J. E. Shaff, S. R. McCouch, D. J. Aneshansley, and L. V. Kochian. Three-dimensional root phenotyping with a novel imaging and software platform. *Plant physiology*, 156(2):455–465, 2011.

[11] P. M. B. Dias, S. Brunel-Muguet, C. Dürr, T. Huguet, D. Demilly, M.-H. Wagner, and B. Teulat-Merah. QTL analysis of seed germination and pre-emergence growth at extreme temperatures in medicago truncatula. *Theoretical and Applied Genetics*, 122(2):429–444, 2011.

[12] L. Duan, W. Yang, C. Huang, and Q. Liu. A novel machine-vision-based facility for the automatic evaluation of yield-related traits in rice. *Plant Methods*, 7(1):44, 2011.

[13] A. A. Gitelson, Y. Zur, O. B. Chivkunova, and M. N. Merzlyak. Assessing carotenoid content in plant leaves with reflectance spectroscopy. *Photochemistry and photobiology*, 75(3):272–281, 2002.

[14] M. R. Golzarian, R. A. Frick, K. Rajendran, B. Berger, S. Roy, M. Tester, and D. S. Lun. Accurate inference of shoot biomass from high-throughput images of cereal plants. *Plant Methods*, 7(1):2, 2011.

[15] H. Grahn and P. Geladi. *Techniques and applications of hyperspectral image analysis*. John Wiley & Sons, 2007.

[16] P. Grassini, K. M. Eskridge, and K. G. Cassman. Distinguishing between yield advances and yield plateaus in historical crop production trends. *Nature Communications*, 4, 2013.

[17] E. Hamuda, M. Glavin, and E. Jones. A survey of image processing techniques for plant extraction and segmentation in the field. *Computers and Electronics in Agriculture*, 125:184–199, 2016.

[18] V. Hoyos-Villegas, J. Houx, S. Singh, and F. Fritschi. Ground-based digital imaging as a tool to assess soybean growth and yield. *Crop Science*, 54(4):1756–1768, 2014.

[19] G. Jeon. Color image enhancement by histogram equalization in heterogeneous color space. *Int. J. Multimedia Ubiquitous Eng*, 9(7):309–318, 2014.

[20] G. Kindlmann and J. W. Durkin. Semi-automatic generation of transfer functions for direct volume rendering. In *Proceedings of the 1998 IEEE symposium on Volume visualization*, pages 79–86. ACM, 1998.

[21] M. Klodt and D. Cremers. High-resolution plant shape measurements from multi-view stereo reconstruction. In *European Conference on Computer Vision*, pages 174–184. Springer, 2014.

[22] K. N. Kutulakos and S. M. Seitz. A theory of shape by space carving. In *Computer Vision, 1999. The Proceedings of the Seventh IEEE International Conference on*, volume 1, pages 307–314. IEEE, 1999.

[23] L. Li, Q. Zhang, and D. Huang. A review of imaging techniques for plant phenotyping. *Sensors*, 14(11):20078–20111, 2014.

[24] M. Meroni, M. Rossini, L. Guanter, L. Alonso, U. Rascher, R. Colombo, and J. Moreno. Remote sensing of solar-induced chlorophyll fluorescence: Review of methods and applications. *Remote Sensing of Environment*, 113(10):2037–2051, 2009.

[25] R. F. Muñoz-Huerta, R. G. Guevara-Gonzalez, L. M. Contreras-Medina, I. Torres-Pacheco, J. Prado-Olivarez, and R. V. Ocampo-Velazquez. A review of methods for sensing the nitrogen status in plants: advantages, disadvantages and recent advances. *Sensors*, 13(8):10823–10843, 2013.

[26] A. Paproki, X. Sirault, S. Berry, R. Furbank, and J. Fripp. A novel mesh processing based technique for 3D plant analysis. *BMC Plant Biology*, 12(1):63, 2012.

[27] A. Perez, F. Lopez, J. Benlloch, and S. Christensen. Colour and shape analysis techniques for weed detection in cereal fields. *Computers and electronics in agriculture*, 25(3):197–212, 2000.

[28] J. Rouse Jr, R. Haas, J. Schell, and D. Deering. Monitoring vegetation systems in the great plains with ERTS. 1974.

[29] P. K. Saha, G. Borgefors, and G. S. di Baja. A survey on skeletonization algorithms and their applications. *Pattern Recognition Letters*, 76:3–12, 2016.

[30] D. K. Sahu and M. Parsai. Different image fusion techniques–a critical review. *International Journal of Modern Engineering Research (IJMER)*, 2(5):4298–4301, 2012.

[31] S. M. Seitz, B. Curless, J. Diebel, D. Scharstein, and R. Szeliski. A comparison and evaluation of multi-view stereo reconstruction algorithms. In *Computer vision and pattern recognition, 2006 IEEE Computer Society Conference on*, volume 1, pages 519–528. IEEE, 2006.

[32] J. Solomon and B. Rock. Imaging spectrometry for earth remote sensing. *Science*, 228(4704):1147–1152, 1985.

[33] B. Somers, G. P. Asner, L. Tits, and P. Coppin. Endmember variability in spectral mixture analysis: A review. *Remote Sensing of Environment*, 115(7):1603–1616, 2011.

[34] S. Sural, G. Qian, and S. Pramanik. Segmentation and histogram generation using the HSV color space for image retrieval. In *Image Processing. 2002. Proceedings. 2002 International Conference on*, volume 2, pages II–II. IEEE, 2002.

[35] O. Sytar, M. Brestic, M. Zivcak, K. Olsovska, M. Kovar, H. Shao, and X. He. Applying hyperspectral imaging to explore natural plant diversity towards improving salt stress tolerance. *Science of The Total Environment*, 578:90–99, 2017.

[36] H. Wang, W. Zhang, G. Zhou, G. Yan, and N. Clinton. Image-based 3D corn reconstruction for retrieval of geometrical structural parameters. *International Journal of Remote Sensing*, 30(20):5505–5513, 2009.

[37] B. Ward, J. Bastian, A. van den Hengel, D. Pooley, R. Bari, B. Berger, and M. Tester. A model-based approach to recovering the structure of a plant from images. In *European Conference on Computer Vision*, pages 215–230. Springer, 2014.

[38] Q. Wu, D. Zhu, C. Wang, Z. Ma, D. Zhang, K. Chen, and J. Wang. The detection of chlorophyll content for salt stress of the wheat seedling by hyperspectral imaging. In *International Symposium on Photoelectronic Detection and Imaging 2011*, pages 81931D–81931D. International Society for Optics and Photonics, 2011.

[39] K.-Q. Yu, Y.-R. Zhao, X.-L. Li, Y.-N. Shao, F. Liu, and Y. He. Hyperspectral imaging for mapping of total nitrogen spatial distribution in pepper plant. *PloS one*, 9(12):e116205, 2014.